

# Energy & Environmental Science

Accepted Manuscript

This article can be cited before page numbers have been issued, to do this please use: G. Wu, A. Li, H. Subramaniam, X. Wu, L. Wang, J. Li, F. F. Yun and T. Mori, *Energy Environ. Sci.*, 2026, DOI: 10.1039/D6EE01515H.



This is an Accepted Manuscript, which has been through the Royal Society of Chemistry peer review process and has been accepted for publication.

Accepted Manuscripts are published online shortly after acceptance, before technical editing, formatting and proof reading. Using this free service, authors can make their results available to the community, in citable form, before we publish the edited article. We will replace this Accepted Manuscript with the edited and formatted Advance Article as soon as it is available.

You can find more information about Accepted Manuscripts in the [Information for Authors](#).

Please note that technical editing may introduce minor changes to the text and/or graphics, which may alter content. The journal's standard [Terms & Conditions](#) and the [Ethical guidelines](#) still apply. In no event shall the Royal Society of Chemistry be held responsible for any errors or omissions in this Accepted Manuscript or any consequences arising from the use of any information it contains.

## Broader context statement

Recovering low-grade waste heat is important for improving energy efficiency, yet many thermoelectric materials still suffer from a mismatch between near-room-temperature and mid-temperature performance. N-type  $\text{Mg}_3\text{Sb}_2$ -based materials are particularly promising because of their cost and mid-temperature potential, but their near-room-temperature transport is often limited by grain-boundary scattering. This work shows that a multifunctional  $\text{CuGaTe}_2$  additive can be used to simultaneously reconfigure the grain-boundary spectrum and generate in-situ Cu-Ga-rich precipitates, thereby improving electrical transport near room temperature while retaining strong phonon scattering at higher temperatures. The result broadens the temperature-window performance. More generally, these results suggest that coordinated regulation of grain-boundary character and precipitates architecture can be an effective route for designing thermoelectric materials that operate efficiently over practical temperature gradients relevant to waste-heat harvesting.



# Strain-mediated grain-boundary reconstruction unlocks high near-room-temperature thermoelectric performance in $\text{Mg}_3\text{Sb}_2$ -based alloy

[View Article Online](#)

Gang Wu<sup>1,3</sup>, Airan Li<sup>1,3</sup>, Harish Subramaniam<sup>1</sup>, Xinzhi Wu<sup>1</sup>, Longquan Wang<sup>1</sup>, Jiankang Li<sup>1,2</sup>, Fei Frank Yun<sup>1</sup>, Takao Mori<sup>1,2\*</sup>

<sup>1</sup> Research Center for Materials Nanoarchitectonics (MANA), National Institute for Materials Science (NIMS), Tsukuba, 305-0044, Japan.

<sup>2</sup> Graduate School of Pure and Applied Science, University of Tsukuba, 1-1-1 Tennodai, Tsukuba, Ibaraki 305-8671, Japan.

<sup>3</sup> These authors contributed equally to this work.

Corresponding author, email: MORI.Takao@nims.go.jp

## Abstract

Achieving high thermoelectric efficiency across wide temperature range, including near room temperature, within a single  $\text{Mg}_3\text{Sb}_2$ -based material remains challenging, because the microstructures that favor low-temperature charge transport often conflict with those required for phonon suppression. Here we demonstrate that subtle lattice perturbations can steer a strain-mediated grain-boundary spectrum reconstruction in  $\text{Mg}_3\text{Sb}_2$ -based system. The grain-boundary spectrum reconfiguration markedly weakens grain-boundary potential barriers and alleviates carrier scattering by raising the fraction of coherent twin boundaries, restoring the power factor near room temperature. Within the same processing window, the multifunctional  $\text{CuGaTe}_2$  additive also undergoes composition-partitioning, yielding uniformly dispersed in-situ Cu-Ga-rich intermetallic phase together with point defects. The resulting multi-length-scale defect landscape provides broadband phonon scattering and suppresses lattice thermal conductivity toward the diffusion limit. Consequently, the optimized alloy delivers an exceptional  $ZT_{\text{ave}}$  of 1.3 at  $\Delta T=250$  K, that exceeds state-of-the-art n-type  $\text{Bi}_2\text{Te}_3$ , while maintaining  $ZT_{\text{ave}}=1.59$  from 300-723 K with a peak  $ZT$  of 2.08 at 623 K. Device demonstrations further validate the materials-level advantages with 8% for the assembled TE module ( $\Delta T=300$  K) and 12.4% for a single-leg generator ( $\Delta T=400$  K). These results indicate that grain-boundary spectrum reconstruction can serve as an effective route to improve near-room-



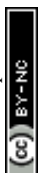
temperature performance and help narrow the performance gap between the near-room- and mid-temperature regimes in n-type  $\text{Mg}_3\text{Sb}_2$  for wide-ranging waste-heat recovery.

View Article Online  
DOI: 10.1039/D6EE01515H

## Introduction

During fossil fuel energy conversion, about two-thirds of the generated energy cannot be utilized efficiently and is dissipated as thermal losses, especially within the room- to intermediate-temperature range, where conventional heat engines are incapable of efficiently harvesting this heat energy.<sup>[1-4]</sup> Thermoelectric (TE) materials, which are capable of directly converting heat into electricity via Seebeck effect without generating any pollutants, have aroused widespread interest. The dimensionless figure of merit ( $ZT$ ) of materials dictates the TE conversion efficiency ( $\eta$ ), where  $ZT$  is governed by three interrelated parameters: electrical conductivity ( $\sigma$ ), Seebeck coefficient ( $S$ ) and thermal conductivity ( $\kappa_{\text{tot}}$ ). Integrating high power factor ( $S^2\sigma$ ) with low thermal conductivity is essential for high  $ZT$  value.<sup>[5, 6]</sup> However, designing TE materials that orchestrate a synergistic optimization between electronic and phonon transport across a broad temperature range remains a formidable challenge.<sup>[7, 8]</sup>

Recently,  $\text{Mg}_3(\text{Sb}, \text{Bi})_2$ -based materials have emerged as compelling candidates for commercial applications, combining earth-abundant constituents with excellent n-type performance and strong potential for scalable commercialization.<sup>[9-15]</sup> The electronic band alignment and lattice dynamics of  $\text{Mg}_3(\text{Sb}, \text{Bi})_2$  can be effectively tuned by adjusting the composition either Sb or Bi.<sup>[16, 17]</sup> Normally, the Bi/Sb ratio not only tunes electronic transport but also dictates the intrinsic trade-off between performance and stability in  $\text{Mg}_3(\text{Sb}, \text{Bi})_2$  materials.<sup>[18-20]</sup> Bi-rich compositions, such as  $\text{Mg}_3\text{Bi}_{1.5}\text{Sb}_{0.5}$ , exhibit excellent near-room-temperature performance due to their narrow band gap and low density-of-states effective mass, but its higher formation energy and severe bipolar effect above 400 K undermine the stability and TE performance.<sup>[21, 22]</sup> In contrast, Sb-rich compositions like  $\text{Mg}_3\text{Sb}_{1.5}\text{Bi}_{0.5}$  deliver high performance in the mid-temperature range, while their TE performance near room temperature remains suboptimal.<sup>[23, 24]</sup> For practical TE devices, achieving high and stable efficiency across the full temperature span is crucial.<sup>[25, 26]</sup> Bridging this performance gap, by extending the high efficiency of Sb-rich  $\text{Mg}_3(\text{Sb}, \text{Bi})_2$  toward the low-temperature regime, is essential to push forward its application.



The relatively low power factor of Mg<sub>3</sub>Sb<sub>2</sub>-based materials near room temperature mainly arises from carrier mobility degradation caused by strong grain boundary (GB) scattering, which reduces the average power factor in the near-room-temperature range. Therefore, mitigating GB scattering is key to enhancing their near-room-temperature thermoelectric performance. According to the Seto's model,<sup>[30]</sup> the mobility can be expressed as,

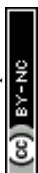
$$\mu_{\text{GB}} = Le \left( \frac{1}{2\pi m^* k_B T} \right)^{\frac{1}{2}} \exp \left( \frac{-E_b}{k_B T} \right) \quad (1)$$

where  $L$ ,  $e$ ,  $m^*$ ,  $k_B$  and  $E_b$  represent the grain size, electron charge, density-of-states effective mass, Boltzmann constant and potential barrier height, respectively. Thus, the carrier mobility is primarily governed by the grain size and potential barrier height. Traditionally, the approaches of enlarging grain size and thereby reducing boundary density, such as long time annealing or liquid phase sintering, enhance the carrier mobility.<sup>[31-34]</sup> However, this way may adversely affect  $\kappa_{\text{lat}}$ . To directly reduce the potential barrier height  $E_b$  seems to be a more attractive strategy. Additionally, the potential barrier height can be expressed as,<sup>[35]</sup>

$$E_b = \frac{e^2 Q_t^2}{8N\epsilon_{\text{st}}} \quad (2)$$

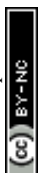
where  $Q_t$ ,  $N$  and  $\epsilon_{\text{st}}$  are the trapping states, concentration of impurity atoms and static dielectric permittivity. The barrier at high angle grain boundaries is typically three to five times larger than that at low angle boundaries because of larger number of trapping states.<sup>[36, 37]</sup> Conversely, twin boundaries (TB) are characterized by coherent atomic arrangements and minimal electronic potential perturbation, which is regarded as electron transparent yet phonon opaque interfaces.<sup>[38-40]</sup> Thus, increasing the fraction of TBs while reducing high angle grain boundaries to reduce the potential barrier height serves as an effective approach to reconcile electrical and thermal transport.

In addition to GB scattering, lower  $\kappa_{\text{lat}}$  is also crucial pathway for achieving high performance. Although Mg<sub>3</sub>Sb<sub>2</sub>-based material exhibits intrinsically low  $\kappa_{\text{lat}}$  due to its complex bonding, it still remains significantly higher than the theoretical minimum predicted by the phonon diffusion limit, leaving substantial room for further thermal optimization. A widely used route is nanoscale structural modulation through controlling defect or second-phase size, spatial dispersion and interface coherency to broaden phonon scattering over a wide spectral window.<sup>[41-43]</sup> However, the



central obstruction is to introduce such phonon-blocking architectures without undermining electrical transport. Sustaining high thermoelectric performance across wide temperature ranges especially for near-room region in  $\text{Mg}_3\text{Sb}_2$  system remains a central challenge. Addressing this limitation is vital for enabling low-cost and scalable thermoelectric power generation.

In this work, we show that a  $\text{CuGaTe}_2$ -enabled strain-mediated grain-boundary spectrum reconstruction provides a distinct route to improve near-room-temperature performance while retaining competitive mid-temperature behaviour in  $\text{Mg}_3\text{Sb}_2$ -based system. Rather than relying on grain coarsening to simply reduce boundary density, which may compromise phonon transport or processing control, the additive introduces localized lattice perturbations that reconfigure the grain-boundary spectrum, raising the fraction of coherent twin boundaries and reducing the high-barrier boundaries. This reconstruction effectively mitigates grain boundary scattering and lowering  $E_b$ , thereby restoring the power factor near room temperature. Notably, during ball milling and subsequent sintering, the  $\text{CuGaTe}_2$  additive undergoes partial interdiffusion and local redistribution of Cu, Ga and Te, which generates processing-induced compositional fluctuations. Under Te-deficient conditions, these redistributed species subsequently partition, giving rise to the in-situ Cu-Ga-rich precipitates and associated point-defect structures, serving as broad-scale phonon-scattering centers and reducing  $\kappa_{\text{lat}}$  to  $0.49 \text{ W m}^{-1} \text{ K}^{-1}$  at room temperature. A schematic representation of the mechanism is displayed in Figure 1a. As a result, the  $\text{Mg}_3\text{Sb}_2$ -based material achieves a superior average  $ZT$  ( $ZT_{\text{ave}}$ ) of 1.3 at  $\Delta T=250 \text{ K}$ , surpassing most reported n-type  $\text{Bi}_2\text{Te}_3$  and rivalling  $\text{Mg}_3\text{Bi}_2$ -based alloys. Moreover, a  $ZT_{\text{ave}}$  of 1.59 is maintained across  $300\sim 723 \text{ K}$ , demonstrating superiority in the mid-temperature regime at the same time, shown in Figure 1b. In addition, a module paired with p-type  $\text{MgAgSb}$  delivers 8% conversion efficiency, exceeding the traditional  $\text{Bi}_2\text{Te}_3$ -based module, and a single TE-leg generator reaches 12.4% at  $\Delta T=400 \text{ K}$ , confirming its strong device-level competitiveness under the same temperature difference, as shown in Fig. 1c-d. This strategy establishes grain-boundary spectrum reconstruction as an effective lever to enable high near-room-temperature performance and bridge the the performance-gap challenge in n-type  $\text{Mg}_3\text{Sb}_2$  alloys, offering promising prospects for wide-ranging waste-heat recovery.





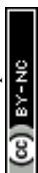
## Results

View Article Online  
DOI: 10.1039/D6EE01515H

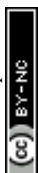
### Strain-mediated grain-boundary spectrum reconstruction optimizing near-room-temperature transport.

Figure S1a presents the powder XRD patterns of  $\text{Mg}_{3.2(1-x)}\text{Cu}_x\text{Ga}_x\text{Sb}_{1.5(1-x)}\text{Bi}_{0.5(1-x)}\text{Te}_{2x}$  ( $x=0, 0.003, 0.005, 0.007, 0.009$ ) samples at room temperature, where all the diffraction peaks are consistent with the  $\text{Mg}_3\text{Sb}_2$ -type phase (JCPDS#03-0375), indicating a single-phase structure without detectable impurities within the sensitivity of XRD. The enlarged view of the (101) peaks reveal a slight shift toward lower diffraction angles at low doping contents, followed by a reverse shift at higher doping levels. The refined lattice parameters in Figure S1b-c show a similar trend. The initial lattice expansion results from the incorporation of atoms into interstitial positions,<sup>[58, 69]</sup> whereas the subsequent contraction is attributed to the segregation of Cu-Ga-rich nanoprecipitates at higher doping levels which will be discussed later.

Given XRD patterns revealed above, the effect of the additive  $\text{CuGaTe}_2$  incorporation on charge transport is further analyzed. GB scattering is a major limiting factor for the electrical transport of  $\text{Mg}_3\text{Sb}_2$ -based materials, particularly near room temperature. The thermoelectric performance of the pristine sample is shown in Figure S2. With increasing temperature, it undergoes an N-P transition. As shown in Figure 2a, with increasing doping content, the dominant carrier scattering mechanism gradually shifts from GB scattering toward acoustic phonon scattering, and temperature-dependent exponent varies from  $T^{-0.2}$  for the  $x = 0.003$  to  $T^{-0.78}$  for the  $x = 0.009$  sample. Compared with the only Te-doped counterparts reported previously,<sup>[9, 58]</sup> the samples after the additive incorporation exhibit a markedly weaker GB scattering. In addition, to further clarify the role of the additive, we also prepare a Te-only doped sample at the same preparation process, whose performance is presented in Figure S3, and find pronounced GB scattering near room temperature. In addition, we plot  $\ln(\sigma T^{1/2})$  as a function of  $(1/k_B T)$  and fit the approximately linear near-room-temperature region to estimate the apparent  $E_b$  for each composition. As we can see from Figure S4, the  $E_b$  of the pristine sample is 34 meV, which is similar to the reported value.<sup>[9, 67]</sup> After  $\text{CuGaTe}_2$  incorporation, the fitted  $E_b$  is markedly reduced compared with the Te-only doped sample, which quantitatively supports our original conclusion that the additive weakens the GB blocking effect. By the way, for the heavily added  $x=0.009$  sample, the fitted near-room-temperature region no longer shows a



physically meaningful negative slope in the Seto plot. The nearly flat slope for  $x=0.009$  indicates that the simple activated-barrier description is no longer strictly applicable. While this does not weaken our conclusion, the quantitative analysis of the compositions is already sufficient to demonstrate that  $\text{CuGaTe}_2$  incorporation substantially lowers the grain-boundary potential barrier. Generally, reduction of GB scattering in  $\text{Mg}_3\text{Sb}_2$ -based materials is obtained by grain coarsening. For instance, Liu *et al.* improves the performance of n-type  $\text{Mg}_3\text{Sb}_{1.5}\text{Bi}_{0.5}$  by doping a small amount of Cu. That work proposes two major effects of Cu addition: interstitial Cu in the lattice, which modifies the phonon structure and suppresses lattice thermal conductivity, and grain-boundary complexion engineering associated with  $\text{Mg}_2\text{Cu}$  eutectic wetting to enhance the grain growth.<sup>[58]</sup> And Lei *et al.* is deliberately introduced as a nano-sintering aid at grain boundaries to promote grain growth. The average grain size increases up to  $23.7\ \mu\text{m}$ , which dramatically suppresses the grain-boundary scattering and improves the carrier mobility.<sup>[33]</sup> In contrast, the EBSD results in this work displayed in Figure S5 reveal a little change in grain size after additive addition. Based on the statistical results summarized in the Table S1 and Figure S6, the mean grain sizes of the selected samples are  $5.04$ ,  $5.60$ , and  $5.20\ \mu\text{m}$ , the median grain sizes are  $4.54$ ,  $4.88$  and  $4.59\ \mu\text{m}$ , and the standard deviations are  $1.54$ ,  $1.57$  and  $1.47\ \mu\text{m}$  for  $x=0$ ,  $x=0.005$  and  $x=0.009$ , respectively. All these statistical parameters vary only within a small range, indicating that the grain-size distributions remain broadly comparable rather than showing substantial coarsening. Therefore, grain growth may make a limited contribution. Instead, compared with the relatively modest grain-size variation, the evolution in grain-boundary character is much more pronounced, which will be discussed later. According to Seto's grain boundary potential barrier model,<sup>[30]</sup> the observed behavior can be attributed to a reduction in the density of trapping states, which lowers the potential barrier height ( $E_b$ ).



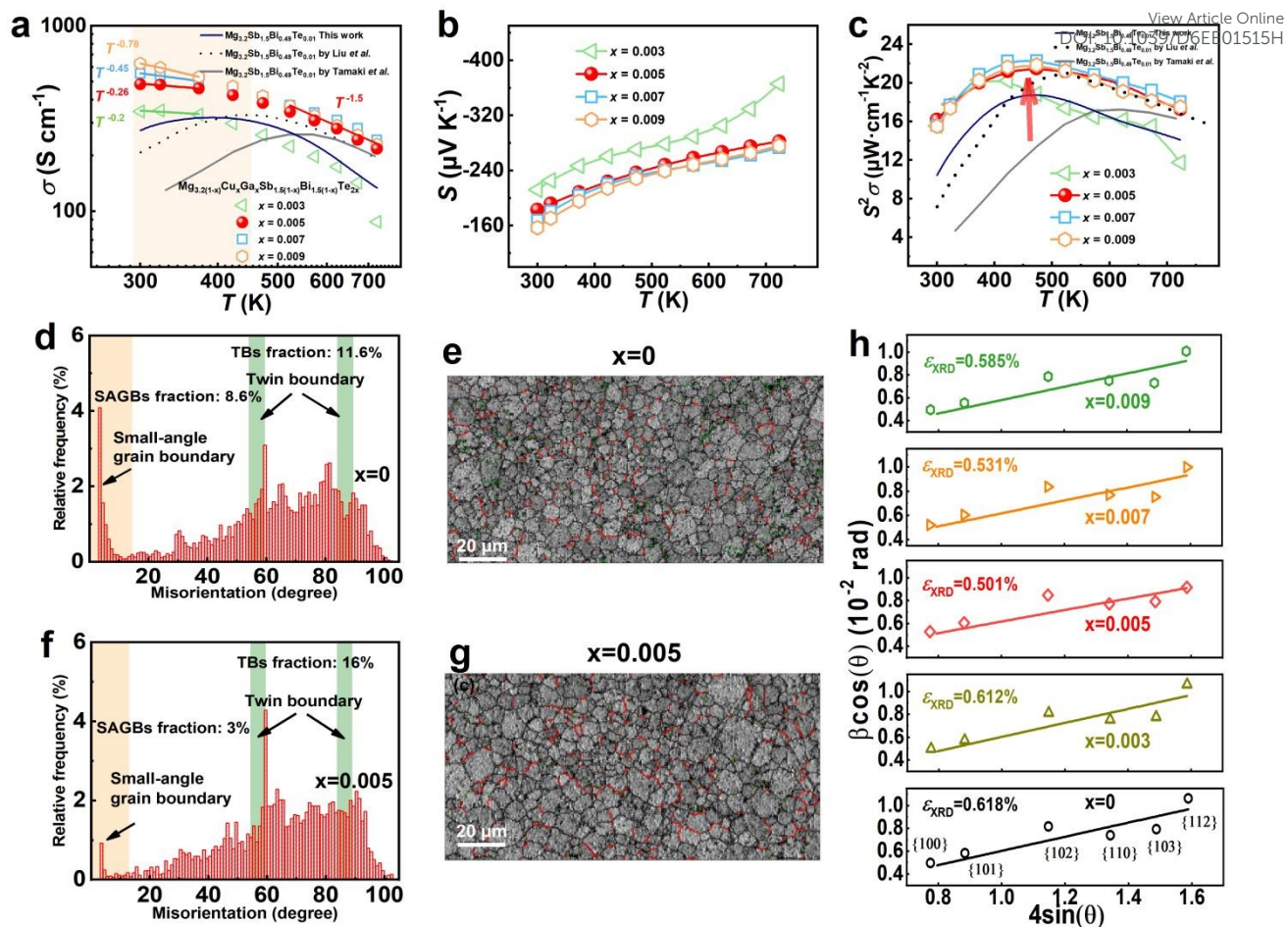


**Figure 2** The temperature-dependent electrical transport properties and microstructural evolution. The temperature-dependent electrical transport properties of  $\text{Mg}_{3.2(1-x)}\text{Cu}_x\text{Ga}_x\text{Sb}_{1.5(1-x)}\text{Bi}_{0.5(1-x)}\text{Te}_{2x}$  samples, **a** electrical conductivity, **b** Seebeck coefficient, **c** power factor. The grain misorientation distributions and corresponding morphology maps for **d-e**  $x=0$  and **f-g**  $x=0.005$  samples. TBs are marked in red, and SAGBs are shown in green. **h** The internal strain analysis of samples.

The Seebeck coefficients of samples as a function of temperature are shown in Figure 2b. All samples exhibit negative Seebeck coefficient value and it increases monotonically with temperature, confirming n-type conduction behavior. With increasing additive content, the value of the Seebeck coefficient gradually decreases, primarily owing to the rise of carrier concentration ( $n$ ), shown in Figure S7. According to the single parabolic band model,<sup>[70]</sup> the relationship between  $n$  and  $S$  is plotted in Figure S8, revealing a moderate increase in the density of states effective mass. This trend may be related to a slight perturbation of the electronic structure induced by Ga incorporation. Similar behavior has been documented previously.<sup>[71]</sup> As a result, owing to effectively weakened GB scattering, sample's power factor achieves a

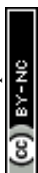


remarkable enhancement near room temperature Figure 2c, ensuring a more balanced performance across a broad temperature range.

View Article Online  
DOI: 10.1039/D6EE01515H

To elucidate the origin of the reduced GB scattering, the structural evolution of samples is systematically examined. The EBSD analysis is performed displayed in Figure 2d-g and Figure S9. In  $\text{Mg}_3(\text{Sb, Bi})_2$ -based alloys, two representative twin modes form under different stress states, compression twins with a  $56^\circ$  misorientation and extension twins with a  $86^\circ$ , where the rotations are both at the  $\langle 11\bar{2}0 \rangle$  axis. From the EBSD results, the grain boundary network undergoes significant reconstruction, accompanied by a marked increase in twin boundaries (TBs). Coherent TBs introduce far less lattice disorder than general grain boundaries, since their lattice mismatch is considerably smaller. TBs are closely correlated with strain relaxation. Williamson-Hall analysis based on XRD, as shown in Figure 2h, provides a spatially averaged descriptor of diffraction-peak-broadening-related microstrain, and thus may approximately reflect the evolution of average lattice distortion. The calculation details are provided in the Supporting Information. The extracted  $\varepsilon_{\text{XRD}}$  is regarded as a spatially averaged parameter, especially in the present defect-rich system where dislocations, small-angle grain boundaries and precipitate-related interfaces may all contribute to peak broadening. Nevertheless, the overall trend of  $\varepsilon_{\text{XRD}}$  remains broadly consistent with the EBSD-observed grain-boundary spectrum evolution and defect-state changes. Specifically, the reduced  $\varepsilon_{\text{XRD}}$  in the optimized sample is interpreted as being consistent with a lower average lattice distortion, whereas the slight increase at higher additive content may be associated with the introduction of more incoherent interfaces due to precipitate coarsening. These results are considered together with the observed changes in twin-boundary fraction, KAM and dislocation density. The coarser precipitates, KAM and dislocation density will be discussed latter Therefore, rather than relying on the Williamson-Hall analysis alone, the combined evidence is interpreted as being broadly consistent with a strain-mediated grain-boundary spectrum reconstruction in this work.

Normally, the presence of small angle grain boundaries (SAGBs) formed by dislocation clusters, along with semi-coherent interfaces and dopant-induced lattice distortions, could result in internal strain. Such accumulated strain energy may provide a thermodynamic driving forces for strain-mediated microstructural reorganization, during which low energy coherent twins preferentially form and partially replace high energy grain boundaries, leading to a pronounced increase in the fraction of TBs and strain relaxation. In Figure S10, we can also see a higher density of TBs in the  $x=0.005$  sample at the magnified misorientation



analysis. In addition, the lower dislocation density and reduced Kernel Average Misorientation (KAM) values in the  $x=0.005$  sample shown in Figure S11-12 are consistent with the decreased proportion of SAGBs. Consequently, this strain-mediated grain-boundary spectrum reconstruction increases the fraction of coherent TBs while reducing high angle grain boundaries with high potential barrier height, thereby lowering the grain boundary scattering and optimizing the electrical transport near room temperature. To further illustrate the function of the additive  $\text{CuGaTe}_2$ , the Cu-Te control sample with the similar nominal additive level is prepared as shown in Figure S13-14. In sharp contrast to the  $\text{CuGaTe}_2$ -doped samples, the Cu-Te control exhibits pronounced grain coarsening, whereas the twin boundary fraction remains essentially unchanged. Therefore, the weakened GB scattering is consistent with the grain-growth route. These comparisons indicate that Cu incorporation alone can indeed mitigate GB scattering via grain coarsening, but it does not reproduce the characteristic microstructural response observed with  $\text{CuGaTe}_2$  addition. Therefore, the near-room-temperature transport improvement in the  $\text{CuGaTe}_2$  case is consistent with a strain-mediated grain-boundary spectrum reconstruction that promotes twin-boundary formation and reduces high angle grain boundaries with high potential barrier height.

## Broad-scale in-situ nanoprecipitates for phonon scattering and wide range $ZT$ enhancement.

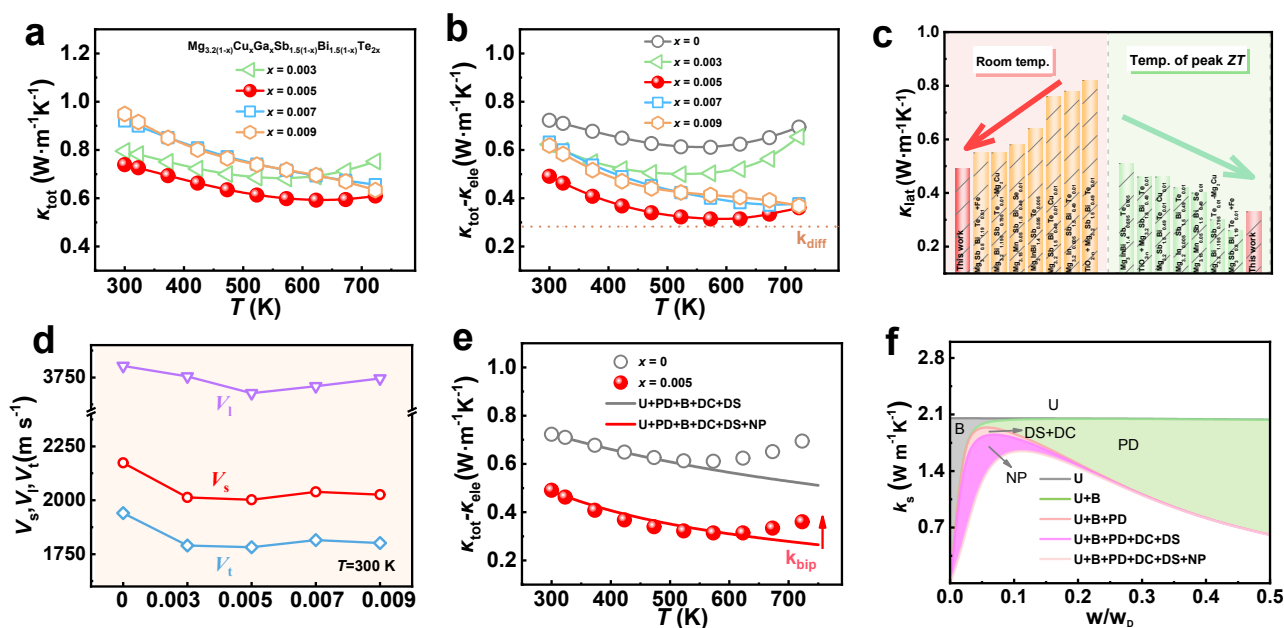


**Figure 3 The temperature-dependent thermal transport properties.** **a**  $\kappa_{\text{tot}}$ , **b**  $\kappa_{\text{tot}} - \kappa_{\text{ele}}$ , **c** comparison of  $\kappa_{\text{lat}}$  between this work and previous reports, **d** sound velocities, **e** the combined contributions from  $\kappa_{\text{bip}}$  and  $\kappa_{\text{lat}}$ , **f** frequency-dependent  $\kappa_s$  of the  $x=0.005$  sample at room temperature, modelled using the Debye-Callaway approach.

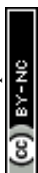
The temperature-dependent thermal transport behaviour is illustrated in Figure 3. As shown in Figure 3a, the  $\kappa_{\text{tot}}$  indicate a nonmonotonic variation with additive content and exhibit that it initially decreases and then increases slightly at higher doping content. This trend mainly reflects the evolution of electronic thermal conductivity ( $\kappa_{\text{ele}}$ ), which is calculated using the Wiedemann-Franz law,  $\kappa_{\text{ele}} = L\sigma T$ , where the Lorenz number  $L$  is estimated through the empirical relationship.<sup>[72]</sup> Owing to the  $\kappa_{\text{ele}}$  is primarily determined by the  $\sigma$ , the contribution of lattice component is obtained by  $\kappa_{\text{tot}} - \kappa_{\text{ele}}$ , shown in Figure 3b. The  $\kappa_{\text{tot}} - \kappa_{\text{ele}}$  values experience a temperature dependence, initially decreasing and then rising at elevated temperatures, mainly due to the activation of bipolar effect. Obviously, the bipolar effect is progressively suppressed with increasing additive content because of the higher carrier concentration inhibiting minority carrier excitation consistent with Figure S7. The lowest  $\kappa_{\text{lat}}$  reaches  $0.31 \text{ W m}^{-1} \text{ K}^{-1}$  for the  $x=0.005$  at 573 K, approaching the theoretical minimum predicted by the phonon diffusion limit. The calculation details of theoretical minimum can be seen in Supporting Information. Compared with the pristine sample, all doped samples display substantially reduced  $\kappa_{\text{lat}}$ , which can be attributed to Cu-induced modification. It can introduce additional phonon channels and weaken the acoustic stiffness of  $\text{Mg}_3\text{Sb}_2$ .<sup>[58]</sup> This can be supported by the reduced sound velocity in Figure 3d and the red-shift of Raman peaks in Figure S15. However, the negligible difference in sound velocity among doped samples suggests that the further variation of  $\kappa_{\text{lat}}$  originates from some other factors rather than intrinsic lattice softening. In addition, the obtained  $\kappa_{\text{lat}}$  in this work, shown in Figure 3c, is lower than most reported n-type  $\text{Mg}_3\text{Sb}_2$ -based materials both at room temperature and extremely near the  $ZT_{\text{max}}$  regime, assuring a balanced performance at a wide temperature range.<sup>[33, 49, 55, 57, 58, 73, 74]</sup>





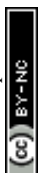
**Figure 4** STEM microstructural analysis of the  $x=0.005$  sample. **a-c** The STEM images showing a high density of lattice defects, with yellow arrows denoting dislocations and red circles highlighting nanoprecipitations. **d-e** EDS elemental distribution maps of Mg, Bi, Sb, Cu, Ga and Te. **f** High-resolution STEM image of nanoprecipitations, and **g** corresponding strain maps derived from geometric phase analysis (GPA), and **h** the inverse FFT (IFFT) image illustrating dislocation distributions.

To further elucidate the phonon transport behavior and microstructural evolution, STEM characterization is performed. From the low-magnification images shown in Figure 4a-c, these reveal numerous dislocations and uniformly dispersed nanoprecipitates across the matrix, consistent with the



multi-region observations in Figure S16. Dislocations represent atomic misalignments and act as two-dimensional line defects capable of effectively scattering mid-frequency phonons. Meanwhile, the nanoprecipitates exhibit a broad size distribution ranging from several nanometers to hundreds of nanometers, contributing to broad scale phonon scattering. Specifically, nanoprecipitates with sizes of a few to tens of nanometers can effectively scatter high-frequency phonons, which has a strong phonon scattering ability, and larger submicron precipitates with weaker scattering strength mainly interact with low-frequency phonons, jointly leading to suppressed  $\kappa_{\text{lat}}$ . In addition, the elemental mapping in Figure 4d-e demonstrates uniform distributions of Mg, Sb, Bi and Te, while Cu and Ga exhibit localized enrichment, confirming the formation of Cu-Ga-rich nanoprecipitates. According to the isothermal Cu-Ga-Te ternary phase diagram and the Cu-Ga binary phase diagram shown in Figure S17-18,  $\text{CuGaTe}_2$  is not expected to remain chemically unchanged under Te-deficient processing conditions. Instead, after partial dissolution and local redistribution during milling or sintering, the local composition can shift toward the Cu-Ga side, making subsequent phase partitioning into Cu-Ga-rich precipitates. As shown in Figure 4f and Figure S16 of the high-resolution TEM images, these nanoprecipitates are located within grains or along grain boundaries, and some of precipitates maintain coherent or semi-coherent interfaces with the matrix. These partially incoherent interfaces could generate the localized lattice strain, as evidenced by the geometric phase analysis (GPA) strain maps Figure 4g. The corresponding Inverse Fast Fourier Transform (IFFT) image in Figure 4h indicates some dislocations surrounding these nanoprecipitates, consistent with the strain distortion. The presence of such broad scale defects, particularly those in nanometer range of precipitates, serves as efficient phonon-scattering centers, thereby contributing to the substantial reduction of  $\kappa_{\text{lat}}$ .

As shown in Figure S19-20, the EPMA is adopted to verify the spatial distribution and composition of precipitates in a wide area on the  $x=0.005$  and  $x=0.009$  samples. Both samples exhibit homogeneous distributions of Mg, Sb, Bi and Te elements, while Cu and Ga show clear localized enrichment, consistent with the STEM observations. Clearly, the Cu-Ga-rich precipitates in the  $x=0.005$  sample are extremely fine whereas those in the  $x=0.009$  sample coarsen significantly to the micrometer scale, which can be attributed to the growth of Cu-Ga intermetallic on further additive addition. Based on the isothermal Cu-Ga-Te ternary phase diagram, the equilibrium composition of  $\text{CuGaTe}_2$  is expected to shift toward the Cu-Ga side under Te-deficient conditions, making the formation of Cu-Ga-rich intermetallic precipitates thermodynamically plausible. Consistently, STEM/EPMA elemental mapping reveals localized enrichment of Cu and Ga, while



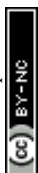
Mg, Sb, Bi and Te remain comparatively homogeneous in the matrix. Moreover, EPMA point analyses in Table S2-3 show very low Te contents in the precipitate-enriched regions, indicating that these precipitates are not Te-rich phases. According to the local Cu/Ga ratios together with the Cu-Ga phase diagram, these precipitates are therefore interpreted as Cu-Ga-rich phases, likely corresponding to Cu-Ga intermetallics.

As confirmed by STEM and EPMA analysis, the presence of broad scale defects, particularly nanometer range of precipitates, act as effective phonon-scattering centers. And these could suppress heat transport over a wide phonon spectrum. At higher doping levels, the coarsening of microscale Cu-Ga-rich precipitates may weaken phonon scattering efficiency, leading to a modest increase in  $\kappa_{\text{lat}}$  shown in Figure 3b, whereas it remains low especially at high temperatures.

To further promote quantify the origin of the decreased  $\kappa_{\text{lat}}$ , the Debye-Callaway model is employed for theoretical analysis:<sup>[75]</sup>

$$\kappa_{\text{lat}} = \frac{k_{\text{B}}}{2\pi^2 v} \left( \frac{k_{\text{B}} T}{\hbar} \right) \int_0^{\theta_{\text{D}}/T} \tau_{\text{tot}}(x) \frac{x^4 e^x}{(e^x - 1)^2} dx \quad (3)$$

where  $x = \hbar\omega/k_{\text{B}}T$ ,  $k_{\text{B}}$ ,  $\hbar$  and  $\tau_{\text{tot}}$  denote the Boltzmann constant, reduced Planck constant, and total phonon relaxation time, respectively. Details are provided in Table S4. In this model, it considers multiple scattering processes, including phonon-phonon Umklapp (U), grain-boundary (B), point-defect (PD), dislocation (DC), strain-induced (DS) and nanoprecipitate (NP) scattering. The sound velocity used in the model corresponds to the experimentally measured values for each sample. As shown in Figure 3e, the simulated  $\kappa_{\text{lat}}$  exhibit good agreement with the experimental data, validating that the reduced sound velocity and presence of nanoprecipitates dominate the suppression of  $\kappa_{\text{lat}}$  in doped samples. As we can see, the  $\kappa_{\text{bip}}$  is also notably mitigated due to enhanced carrier concentration. To gain further insight, the frequency-dependent  $\kappa_{\text{s}}$  for the  $x=0.005$  sample at room temperature is plotted in Figure 3f. As we can see, the low-frequency phonons are mainly scattered by grain boundaries, while the intermediate-frequency phonons are additionally scattered by dislocations and strain fields. In the higher-frequency regime, point defects become particularly effective because their scattering rate increases strongly with phonon frequency. The precipitates with different sizes scatter phonons over different frequency ranges: the larger precipitates mainly scatter lower-frequency phonons, whereas the finer nanoscale precipitates are more effective for higher-frequency phonons. The analysis reveals that nanoprecipitates and point scattering well



contributes to the reduction of  $\kappa_{\text{lat}}$ , consistent with the previous analysis of microstructural evolution. Thus, the broad scale defect network especially the nanoscale precipitates, provides phonon scattering over broad frequency ranges and substantially depresses  $\kappa_{\text{lat}}$ .



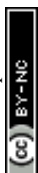
**Figure 5** The thermoelectric performance of  $ZT$  and fabricated single-leg and TE module. **a**  $\mu_w/\kappa_{\text{lat}}$ , **b**  $ZT$ , **c** comparison of  $ZT$  values with representative n-type thermoelectric systems, including  $\text{Bi}_2\text{Te}_3$ -,  $\text{Mg}_3\text{Bi}_2$ - and  $\text{Mg}_3\text{Sb}_2$ -based materials, **d** the measured contact resistance, **e-f**  $I$ - $V$  and  $I$ - $P$  characteristics and conversion efficiency ( $\eta$ ) of the TE module under different temperature differences, **g-h**  $I$ - $V$  and  $I$ - $P$  curves and  $\eta$  of the single-leg generator at various temperature gradients, **i** comparison of conversion efficiency between this work and reported single-leg devices.

As a result, by integrating strain-mediated grain-boundary spectrum reconstruction with the formation of broad-scale in-situ Cu-Ga-rich nanoprecipitates, the additive-enabled effect establishes a synergistic optimization between electron and phonon transport. As shown in Figure 5a, the ratio of weighted mobility ( $\mu_w$ ) to  $\kappa_{\text{lat}}$  provides a comprehensive indicator of the electron and phonon balance in this work. The calculation method of weighted mobility display in Supporting



Information. The values increase markedly after additive incorporation and reach a maximum at  $x=0.005$ , consistent with the previous analysis. Furthermore, a maximum  $ZT$  of 2.08 at 623 K is achieved, while high  $ZT$  values persist throughout the measured temperature range plotted in Figure 5b. By the way, although the  $x=0.009$  sample still retain some beneficial structural evolution for charge transport, the deterioration in thermal transport becomes more significant owing to the coarser precipitates. So, the negative effect on thermal properties outweighs the gain in electrical properties, leading to a slightly lower overall thermoelectric performance than that of the  $x=0.005$  sample. Remarkably, the near room temperature  $ZT$  surpasses that of commercial n-type  $\text{Bi}_2\text{Te}_3$ -based materials and rivals the  $\text{Mg}_3\text{Bi}_2$ -rich counterparts that dominate the room-temperature regime displayed in Figure 5c.<sup>[33, 47, 52, 54, 55, 57-60, 74, 76-80]</sup> This achievement effectively bridges the long-standing performance gap between  $\text{Mg}_3\text{Sb}_2$ -rich mid-temperature materials and  $\text{Mg}_3\text{Bi}_2$ -rich near-room-temperature systems, realizing a broad range high TE performance window from room temperature to above 700 K. To verify reproducibility, multiple samples of  $x=0.005$  are prepared and tested, showing highly consistent TE properties plotted in Figure S21.

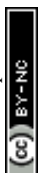
These strategies, including strain-mediated grain-boundary spectrum reconstruction and broad scale in-situ Cu-Ga-rich nanoprecipitates, orchestrate broad-range thermoelectric performance and highlight the effectiveness. To further validate the practical potential of the optimized  $\text{Mg}_{3.2(1-x)}\text{Cu}_x\text{Ga}_x\text{Sb}_{1.5(1-x)}\text{Bi}_{0.5(1-x)}\text{Te}_{2x}$  materials, a TE module and single-leg device are fabricated. Primarily, the finite element numerical simulation is carried out to refine the device architectures and determine the most efficient structural configuration. The refined geometries are plotted in Figure S22-23. As shown in Figure 5d, the contact resistance between the TE materials and barrier layer is remarkably low, suggesting well electrical coupling at the interface. In addition, the interfacial structure, indicating by SEM and its elemental mapping shown in Figure S24, reveals continuous interface without detectable pores or elemental diffusion. The well bonded and chemically stable interfaces ensure the thermal and mechanical reliability for TE device. The TE conversion behaviour of fabricated devices is also systematically evaluated. Figure 5e-h display the  $I$ - $V$  and  $I$ - $P$  characteristics and conversion efficiency ( $\eta$ ) of the TE module and single leg generator under different temperature differences. As we can see, the open circuit voltage ( $V$ ) of the TE module increases progressively with the applied temperature difference, consistent with the Seebeck effect. The corresponding  $I$ - $P$  curves exhibit the typical parabolic dependence, and it reaches its maximum value when the external resistance is the same as the



internal resistance. The internal resistance determined from the slope of the  $I$ - $V$  curve increase slightly with temperature due to the decrease in electrical conductivity, shown in Figure S25-26. Meanwhile, as current increases, the output heat flow also rises, reflecting the combined contribution of Joule and Peltier effects. Thus, a module paired with p-type MgAgSb achieves a conversion efficiency of 8% at  $\Delta T=300$  K, surpassing conventional  $\text{Bi}_2\text{Te}_3$ -based modules in the near-room-temperature range. For the reproducibility, we have remeasured the fabricated two-pair module displayed in Figure S27. And there is a good reproducibility in their efficiency performance under the same test conditions. In addition, a single-leg generator attains  $\eta=12.4\%$  at  $\Delta T=400$  K. As illustrated in Figure 5i,<sup>[81-85]</sup> the comparison of single-leg efficiencies across various TE systems highlights the superior performance of our device at the same testing temperature, confirming its feasibility for practical power generation. These device-level achievements convincingly demonstrate the effectiveness of the strain-mediated grain-boundary spectrum reconstruction and in-situ nanoprecipitates strategy, which successfully bridges the long-standing performance gap between near room and mid-temperature TE regimes, enabling efficient power generation across a broad temperature window.

## Discussion

In summary, this work demonstrates that strain-mediated grain-boundary spectrum reconstruction and broad scale in-situ nanoprecipitates can serve as an effective route to reconcile near-room-temperature and mid-temperature thermoelectric performance in n-type  $\text{Mg}_3\text{Sb}_2$ . By utilizing  $\text{CuGaTe}_2$  as a multifunctional additive, subtle lattice perturbations drive a reconfiguration of the grain boundary spectrum, markedly increasing the fraction of coherent twin boundaries and reducing grain-boundary potential barriers. This grain boundary spectrum engineering restores power factor especially near room temperature regime. Notably, the processing-induced compositional fluctuations give rise to in-situ nanoscale phase partitioning forming multi-length-scale phonon-scattering architectures that suppress lattice thermal conductivity to  $0.49 \text{ W m}^{-1} \text{ K}^{-1}$  without degrading electronic transport. As a result, the  $\text{Mg}_3\text{Sb}_2$  system yields an impressive average  $ZT$  of 1.3 at  $\Delta T=250$  K, surpassing most reported n-type  $\text{Bi}_2\text{Te}_3$ -based materials near room temperature, and maintains a high average  $ZT$  of 1.59 (300-723 K), exhibiting superiority in the mid-temperature regime as well. Moreover, the assembled devices deliver outstanding conversion efficiencies of 8% at  $\Delta T=300$  K and 12.4% at  $\Delta T=400$  K, confirming strong device-level competitiveness. These findings suggest a



potentially useful route to achieve high thermoelectric performance from near room to mid-temperature window for waste-heat recovery applications.

View Article Online  
DOI: 10.1039/D6EE01515H

## Methods

**Sample synthesis.** Polycrystalline samples with nominal compositions of  $\text{Mg}_{3.2(1-x)}\text{Cu}_x\text{Ga}_x\text{Sb}_{1.5(1-x)}\text{Bi}_{0.5(1-x)}\text{Te}_{2x}$  ( $x=0, 0.003, 0.005, 0.007, 0.009$ ) were synthesized from high-purity Mg (4N), Sb (4N), Bi (4N) and  $\text{CuGaTe}_2$  powders, where Cu, Ga and Te were introduced in the form of the ternary additive  $\text{CuGaTe}_2$ . The mixed raw materials were placed in a ball mill and milled for 5 h (SPEX-Sample Prep 8000 Mixer Mill). The milled powders were loaded into a graphite die ( $\phi 10$  mm) in an argon atmosphere and densified by SPS (SPS-1080 System, SPS SYNTEX INC) at 973 K under 60 MPa for 20 minutes. The p-type  $\text{MgAgSb}$  material was synthesized with a nominal composition of  $\text{MgAg}_{0.97}\text{Sb}_{0.99}$  (referred to as  $\text{MgAgSb}$ ) using Mg turnings, Ag powder, Sb shots and 0.75wt%  $\text{C}_{18}\text{H}_{36}\text{O}_2$ . All raw materials were weighed based on the target stoichiometry and sealed in a ball-milling jar under an argon atmosphere. The mixture was mechanically alloyed for 5 h, followed by vacuum spark plasma sintering at 573 K and 60 MPa for 5 min to obtain the bulk sample. The  $\text{CuGaTe}_2$  powders were self-synthesized by sealing stoichiometric amounts of high-purity Cu (4N), Ga (4N) and Te (4N) in an evacuated quartz tube, followed by heating to 1373 K at a rate of 30 K  $\text{min}^{-1}$ , holding for 10 hours, and then furnace-cooling to room temperature. The phase purity of the obtained  $\text{CuGaTe}_2$  was confirmed by XRD, as shown in Figure S28.

**Measurement and characterization.** The commercial instrument ZEM-3 (ULVAC ZEM-3) was used to test samples'  $\sigma$  and  $S$  at the Helium atmosphere. The  $\kappa_{\text{tot}}$  was derived from  $\kappa_{\text{tot}}=D\rho C_p$ . Here,  $D$  was measured using a Netzsch LFA 467 instrument,  $\rho$  was obtained based on the Archimedes principle, and  $C_p$  was evaluated using the formula  $C_p = 3NR(1 + 1.3 \times 10^{-4} T - 4 \times 10^3 T^{-2})/M$ .<sup>[86]</sup> Room-temperature carrier concentration ( $n$ ) and carrier mobility ( $\mu$ ) were obtained from Hall-effect measurements performed on a PPMS (Physical Properties Measurement System, Quantum Design).

The samples' structure and microstructural characterizations were performed by X-ray diffraction (SmartLab3, Rigaku), Electron Backscatter Diffraction (EBSD, JSM-7001F, JEOL Inc.), Scanning Electron Microscope (SEM, Hitachi SU4800), Electron Probe Microanalysis (EPMA, JXA-8500F), Raman spectroscopy (inVia, Renishaw) and Scanning Transmission Electron Microscopy (STEM, JEM-ARM-



200F-B). The sound velocity at 300 K was measured using an ultrasonic system (UVM-2, Ultrasonic Engineering Co., Ltd.).

View Article Online  
DOI: 10.1039/D6EE01515H

Unless otherwise stated, the electrical conductivity, Seebeck coefficient, Hall properties and thermal transport properties shown for each composition were obtained from one independently prepared bulk sample. For the optimized composition  $x=0.005$ , multiple independently prepared samples were further characterized in order to verify reproducibility

**TE module fabrication.** A single-leg generator was fabricated using the ball-milled  $\text{Mg}_{3.184}\text{Cu}_{0.005}\text{Ga}_{0.005}\text{Sb}_{1.4925}\text{Bi}_{0.4975}\text{Te}_{0.01}$  powder, sandwiched between Ni foils and 304 stainless-steel foils in a Ni/304 stainless-steel/sample powder/304 stainless-steel/Ni structure, followed by a one-step sintering process. The obtained ingot was cut into dice with dimensions of  $3.4 \times 3.4 \times 6 \text{ mm}^3$ . The two-pair thermoelectric module was assembled using n-type  $\text{Mg}_{3.184}\text{Cu}_{0.005}\text{Ga}_{0.005}\text{Sb}_{1.4925}\text{Bi}_{0.4975}\text{Te}_{0.01}$  legs with dimensions of  $3.5 \times 3.5 \times 6 \text{ mm}^3$  and p-type MgAgSb legs. The conversion efficiency was measured using a Mini-PEM (ADVANCE RIKO, Japan). The properties of p-type MgAgSb were shown in Figure S29. Further descriptions of the simulation procedures can be found in the Supporting Information.

## Data Availability

All data generated or analysed during this study are included in this article (and its supplementary information file).

## Author Contributions Statement

**G.W.:** Conceptualization, Methodology, Investigation, Formal analysis, Data curation, Writing-original draft. **A.L.:** Writing-review and editing. **H.S.I.:** Discussion, Writing-review and editing. **L.W.:** Discussion, Writing-review and editing. **X.W.:** Discussion, Writing-review and editing. **J.L.:** Discussion, Writing-review and editing. **F.Y.:** Discussion, Writing-review and editing. **T.M.:** Conceptualization, Supervision, Writing-review and editing.

## Competing Interests Statement



T. M. and G.W. have filed one Japanese patent application (2025-244532). The remaining authors declare no competing interests.

View Article Online  
DOI: 10.1039/D6EE01515H

## Acknowledgements

This work was supported by JST Mirai Program (JPMJMI19A1, T. M.)

## References

- 1 L. E. Bell, *Science*, 2008, **321**, 1457-1461.
- 2 I. Petsagkourakis, K. Tybrandt, X. Crispin, I. Ohkubo, N. Satoh and T. Mori, *Sci. Technol. Adv. Mater.*, 2018, **19**, 836-862.
- 3 Q. Yan and M. G. Kanatzidis, *Nat. Mater.*, 2022, **21**, 503-513.
- 4 X. L. Shi, J. Zou and Z. G. Chen, *Chem. Rev.*, 2020, **120**, 7399-7515.
- 5 X. L. Shi, N. H. Li, M. Li and Z. G. Chen, *Chem. Rev.*, 2025, **125**, 7525-7724.
- 6 S. Bano, R. Chetty, J. Babu and T. Mori, *Device*, 2024, **2**, 100408.
- 7 T. Hendricks, T. Caillat and T. Mori, *Energies*, 2022, **15**, 2022.
- 8 G. J. Snyder and E. S. Toberer, *Nat. Mater.*, 2008, **7**, 105-114.
- 9 H. Tamaki, H. K. Sato and T. Kanno, *Adv. Mater.*, 2016, **28**, 10182-10187.
- 10 A. Li, C. Fu, X. Zhao and T. Zhu, *Research*, 2020, **2020**, 1934848.
- 11 H. Shang, Z. Liang, C. Xu, J. Mao, H. Gu, F. Ding and Z. Ren, *Research*, 2020, **2020**, 1219461.
- 12 W. Xu, B. A. Al-Maythaly, J. Li, X. Li, L. Fu and B. Xu, *Adv. Funct. Mater.*, 2024, **35**, 2414194.
- 13 P. Zhao, W. Xue, Y. Zhang, S. Zhi, X. Ma, J. Qiu, T. Zhang, S. Ye, H. Mu, J. Cheng, X. Wang, S. Hou, L. Zhao, G. Xie, F. Cao, X. Liu, J. Mao, Y. Fu, Y. Wang and Q. Zhang, *Nature*, 2024, **631**, 777-782.
- 14 H. Yang, P. Xu, B. A. Al-Maythaly, Y. Huang, M. Xu, Y. Hua, W. Zhang, X. Wang, S. Cui, H. Zhu and B. Xu, *Sci. Adv.*, 2026, **12**, ead3783.
- 15 L. Wang, A. Li, X. Wu, J. Li, T. Ohsawa and T. Mori, *Adv. Mater.*, 2025, **37**, e2508270.
- 16 X. Shi, X. Wang, W. Li and Y. Pei, *Small Methods*, 2018, **2**, 1800022.
- 17 S. Ohno, K. Imasato, S. Anand, H. Tamaki, S. D. Kang, P. Gorai, H. K. Sato, E. S. Toberer, T. Kanno and G. J. Snyder, *Joule*, 2018, **2**, 141-154.



- 18 X. Wu, X. Ma, H. Yao, K. Liang, P. Zhao, S. Hou, L. Yin, H. Yang, J. Sui, X. Lin, F. Cao, Q. Zhang and J. Mao, *ACS Appl. Mater. Interfaces*, 2023, **15**, 50216-50224. View Article Online  
DOI: 10.1039/D6EE01515H
- 19 J. Zhang, L. Song, S. H. Pedersen, H. Yin, L. T. Hung and B. B. Iversen, *Nat. Commun.*, 2017, **8**, 13901.
- 20 A. Li, P. Nan, Y. Wang, Z. Gao, S. Zhang, Z. Han, X. Zhao, B. Ge, C. Fu and T. Zhu, *Acta Mater.*, 2022, **239**, 118301.
- 21 Q.-Q. Wang, K.-F. Liu, Y.-Y. Su, X.-C. Liu, Q. Liu, S. Zhou, J. Liu and S.-Q. Xia, *Acta Mater.*, 2023, **255**, 119028.
- 22 S. Xie, X. Wan, Y. Wu, C. Li, F. Yan, Y. Ouyang, H. Ge, X. Li, Y. Liu, R. Wang, M. Y. Toriyama, G. J. Snyder, J. Yang, Q. Zhang, W. Liu and X. Tang, *Adv. Mater.*, 2024, **36**, e2400845.
- 23 J. Mao, J. Shuai, S. Song, Y. Wu, R. Dally, J. Zhou, Z. Liu, J. Sun, Q. Zhang, C. Dela Cruz, S. Wilson, Y. Pei, D. J. Singh, G. Chen, C. W. Chu and Z. Ren, *Proc. Natl. Acad. Sci. U. S. A.*, 2017, **114**, 10548-10553.
- 24 W. Peng, G. Petretto, G.-M. Rignanese, G. Hautier and A. Zevalkink, *Joule*, 2018, **2**, 1879-1893.
- 25 R. Chetty, J. Babu and T. Mori, *Joule*, 2024, **8**, 556-562.
- 26 T. Mori, *Small*, 2017, **13**, 1702013.
- 27 J. J. Kuo, S. D. Kang, K. Imasato, H. Tamaki, S. Ohno, T. Kanno and G. J. Snyder, *Energy Environ. Sci.*, 2018, **11**, 429-434.
- 28 J. J. Kuo, Y. Yu, S. D. Kang, O. Cojocar-Mirédin, M. Wuttig and G. J. Snyder, *Adv. Mater. Interfaces*, 2019, **6**, 1900429.
- 29 J. Mao, Y. Wu, S. Song, Q. Zhu, J. Shuai, Z. Liu, Y. Pei and Z. Ren, *ACS Energy Letters*, 2017, **2**, 2245-2250.
- 30 J. Y. W. Seto, *J. Appl. Phys.*, 1975, **46**, 5247-5254.
- 31 M. Wood, J. J. Kuo, K. Imasato and G. J. Snyder, *Adv. Mater.*, 2019, **31**, e1902337.
- 32 K. Imasato, C. Fu, Y. Pan, M. Wood, J. J. Kuo, C. Felser and G. J. Snyder, *Adv. Mater.*, 2020, **32**, e1908218.
- 33 J. Lei, K. Zhao, J. Liao, S. Yang, Z. Zhang, T. R. Wei, P. Qiu, M. Zhu, L. Chen and X. Shi, *Nat. Commun.*, 2024, **15**, 6588.
- 34 T. Luo, J. J. Kuo, K. J. Griffith, K. Imasato, O. Cojocar-Mirédin, M. Wuttig, B. Gault, Y. Yu and G. J. Snyder, *Adv. Funct. Mater.*, 2021, **31**, 2100258.
- 35 C. Hu, K. Xia, C. Fu, X. Zhao and T. Zhu, *Energy Environ. Sci.*, 2022, **15**, 1406-1422.



- 36 R. Wu, Y. Yu, S. Jia, C. Zhou, O. Cojocaru-Miredin and M. Wuttig, *Nat. Commun.*, 2023, **14**, 719. View Article Online  
DOI: 10.1039/D6EE01515H
- 37 Y. Yu and M. Wuttig, *Nano Res. Energy*, 2023, **2**, e9120057.
- 38 G. Li, J. He, Q. An, S. I. Morozov, S. Hao, P. Zhai, Q. Zhang, W. A. Goddard and G. J. Snyder, *Acta Mater.*, 2019, **169**, 9-14.
- 39 H. Wang, S. Zheng, H. Wu, X. Xiong, Q. Xiong, H. Wang, Y. Wang, B. Zhang, X. Lu, G. Han, G. Wang and X. Zhou, *Small*, 2022, **18**, e2104592.
- 40 A. Zhang, B. Zhang, W. Lu, D. Xie, H. Ou, X. Han, J. Dai, X. Lu, G. Han, G. Wang and X. Zhou, *Adv. Funct. Mater.*, 2018, **28**, 1705117.
- 41 G. Tan, F. Shi, S. Hao, L. D. Zhao, H. Chi, X. Zhang, C. Uher, C. Wolverton, V. P. Dravid and M. G. Kanatzidis, *Nat. Commun.*, 2016, **7**, 12167.
- 42 K. Biswas, J. He, I. D. Blum, C. I. Wu, T. P. Hogan, D. N. Seidman, V. P. Dravid and M. G. Kanatzidis, *Nature*, 2012, **489**, 414-418.
- 43 K. Biswas, J. He, Q. Zhang, G. Wang, C. Uher, V. P. Dravid and M. G. Kanatzidis, *Nat. Chem.*, 2011, **3**, 160-166.
- 44 B. Zhu, X. Liu, Q. Wang, Y. Qiu, Z. Shu, Z. Guo, Y. Tong, J. Cui, M. Gu and J. He, *Energy Environ. Sci.*, 2020, **13**, 2106-2114.
- 45 Y. Liu, Y. Zhang, K. H. Lim, M. Ibanez, S. Ortega, M. Li, J. David, S. Marti-Sanchez, K. M. Ng, J. Arbiol, M. V. Kovalenko, D. Cadavid and A. Cabot, *ACS Nano*, 2018, **12**, 7174-7184.
- 46 B. Zhu, Z.-Y. Huang, X.-Y. Wang, Y. Yu, L. Yang, N. Gao, Z.-G. Chen and F.-Q. Zu, *Nano Energy*, 2017, **42**, 8-16.
- 47 G. Wu, Q. Zhang, X. Tan, Y. Fu, Z. Guo, Z. Zhang, Q. Sun, Y. Liu, H. Shi, J. Li, J. G. Noudem, J. Wu, G. Q. Liu, P. Sun, H. Hu and J. Jiang, *Adv. Mater.*, 2024, **36**, e2400285.
- 48 H. Yang, B. Jia, L. Xie, D. Mao, J. Xia, J. Yang, M. Yuan, Q. Gan, X. Liu, M. Hu, J. Shuai and J. He, *Joule*, 2024, **8**, 2667-2680.
- 49 K. Jin, H. Nie, F. Gao, J. J. Ma, M. Shu, X. Yan, Z. H. Ge, X. Gao, W. Zhao, M. Liu, Y. Yu, J. Ma, B. Xu and L. Fu, *Adv. Funct. Mater.*, 2024, **35**, 2418041.
- 50 K. Yang, X. Li, C. Sun, W. Song, W. Zhao and Q. Zhang, *Adv. Funct. Mater.*, 2024, **34**, 2315886.
- 51 X. Mo, J. Liao, G. Yuan, S. Zhu, X. Lei, L. Huang, Q. Zhang, C. Wang and Z. Ren, *J. Magnes. Alloys*, 2022, **10**, 1024-1032.



- 52 P. Ying, L. Wilkens, H. Reith, N. P. Rodriguez, X. Hong, Q. Lu, C. Hess, K. Nielsch and R. He, *Energy Environ. Sci.*, 2022, **15**, 2557-2566. View Article Online  
DOI: 10.1039/D6EE01515H
- 53 H. Cho, S. Y. Back, N. Sato, Z. Liu, W. Gao, L. Wang, H. D. Nguyen, N. Kawamoto and T. Mori, *Adv. Funct. Mater.*, 2024, **34**, 2407017.
- 54 Z. Liu, W. Gao, H. Oshima, K. Nagase, C. H. Lee and T. Mori, *Nat. Commun.*, 2022, **13**, 1120.
- 55 J. W. Li, H. Gao, Z. Han, J. Yu, H. L. Zhuang, L. Chen, H. Li, Y. Jiang, Z. Wang, Q. Zheng and J. F. Li, *Adv. Mater.*, 2025, **37**, e2503665.
- 56 J. W. Li, Z. Han, J. Yu, H. L. Zhuang, H. Hu, B. Su, H. Li, Y. Jiang, L. Chen, W. Liu, Q. Zheng and J. F. Li, *Nat. Commun.*, 2023, **14**, 7428.
- 57 L. Wang, W. Zhang, S. Y. Back, N. Kawamoto, D. H. Nguyen and T. Mori, *Nat. Commun.*, 2024, **15**, 6800.
- 58 Z. Liu, N. Sato, W. Gao, K. Yubuta, N. Kawamoto, M. Mitome, K. Kurashima, Y. Owada, K. Nagase, C.-H. Lee, J. Yi, K. Tsuchiya and T. Mori, *Joule*, 2021, **5**, 1196-1208.
- 59 X. Chen, H. Wu, J. Cui, Y. Xiao, Y. Zhang, J. He, Y. Chen, J. Cao, W. Cai, S. J. Pennycook, Z. Liu, L.-D. Zhao and J. Sui, *Nano Energy*, 2018, **52**, 246-255.
- 60 J. W. Li, W. Liu, W. Xu, H. L. Zhuang, Z. Han, F. Jiang, P. Zhang, H. Hu, H. Gao, Y. Jiang, B. Cai, J. Pei, B. Su, Q. Li, K. Hayashi, H. Li, Y. Miyazaki, X. Cao, Q. Zheng and J. F. Li, *Adv. Mater.*, 2023, **35**, e2209119.
- 61 Q. Zhang, M. Yuan, K. Pang, Y. Zhang, R. Wang, X. Tan, G. Wu, H. Hu, J. Wu, P. Sun, G. Q. Liu and J. Jiang, *Adv. Mater.*, 2023, **35**, e2300338.
- 62 Y. K. Zhu, Y. Sun, J. Zhu, K. Song, Z. Liu, M. Liu, M. Guo, X. Dong, F. Guo, X. Tan, B. Yu, W. Cai, J. Jiang and J. Sui, *Small*, 2022, **18**, e2201352.
- 63 A. Nozariasbmarz, B. Poudel, W. Li, H. B. Kang, H. Zhu and S. Priya, *iScience*, 2020, **23**, 101340.
- 64 M. Jiang, Y. Fu, Q. Zhang, Z. Hu, A. Huang, S. Wang, L. Wang and W. Jiang, *Nat. Sci. Rev.*, 2023, **10**, nwad095.
- 65 X. Wu, Y. Lin, Z. Han, H. Li, C. Liu, Y. Wang, P. Zhang, K. Zhu, F. Jiang, J. Huang, H. Fan, F. Cheng, B. Ge and W. Liu, *Adv. Energy Mater.*, 2022, **12**, 2203039.
- 66 L. Yin, C. Chen, F. Zhang, X. Li, F. Bai, Z. Zhang, X. Wang, J. Mao, F. Cao, X. Chen, J. Sui, X. Liu and Q. Zhang, *Acta Mater.*, 2020, **198**, 25-34.



- 67 L. Wang, N. Sato, Y. Peng, R. Chetty, N. Kawamoto, D. H. Nguyen and T. Mori, *Adv. Energy Mater.*, 2023, **13**, 2301667. View Article Online  
DOI: 10.1039/D6EE01515H
- 68 J. Li, R. Chetty, Z. Liu, W. Gao and T. Mori, *Small*, 2025, **21**, e2408059.
- 69 X. Yang, H. Ni, X. Yu, B. Cao, J. Xing, Q. Chen, L. Xi, J. Liu, J. Zhang, K. Guo and J.-T. Zhao, *J. Materiomics*, 2024, **10**, 154-162.
- 70 J. Mao, H. S. Kim, J. Shuai, Z. Liu, R. He, U. Saparamadu, F. Tian, W. Liu and Z. Ren, *Acta Mater.*, 2016, **103**, 633-642.
- 71 L. Jiang, S. Tan, R. Chen, J. Xian, H. Li, D. Zhou, H. Kang, Z. Chen, E. Guo and T. Wang, *ACS Appl. Mater. Interfaces*, 2024, **16**, 60197-60207.
- 72 H.-S. Kim, Z. M. Gibbs, Y. Tang, H. Wang and G. J. Snyder, *APL Mater.*, 2015, **3**, 041506.
- 73 F. Zhang, C. Chen, H. Yao, F. Bai, L. Yin, X. Li, S. Li, W. Xue, Y. Wang, F. Cao, X. Liu, J. Sui and Q. Zhang, *Adv. Funct. Mater.*, 2019, **30**, 1906143.
- 74 L. Wang, A. Li, J. Li, N. Kawamoto, D. H. Nguyen and T. Mori, *Nano Energy*, 2025, **137**.
- 75 J. Callaway, *Phys. Rev.*, 1959, **113**, 1046-1051.
- 76 C. Xiong, F. Shi, H. Wang, J. Cai, S. Zhao, X. Tan, H. Hu, G. Liu, J. G. Noudem and J. Jiang, *ACS Appl. Mater. Interfaces*, 2021, **13**, 15429-15436.
- 77 R. Zhai, Y. Wu, T.-J. Zhu and X.-B. Zhao, *Cryst. Growth Des.*, 2018, **18**, 4646-4652.
- 78 J. Peng, D. Liu, S. Bai, Y. Wen, H. Liang, L. Su, X. Qian, D. Wang, X. Gao, Z. Ding, Q. Cao, Y. Pei, B. Qin and L. D. Zhao, *Adv. Energy Mater.*, 2025, **15**, 2404653.
- 79 N. Chen, H. Zhu, G. Li, Z. Fan, X. Zhang, J. Yang, T. Lu, Q. Liu, X. Wu, Y. Yao, Y. Shi and H. Zhao, *Nat. Commun.*, 2023, **14**, 4932.
- 80 X. Li, C. Chen, L. Yin, X. Wang, J. Mao, F. Cao and Q. Zhang, *Energy Environ. Sci.*, 2023, **16**, 6147-6154.
- 81 Y. Jiang, J. Dong, H. L. Zhuang, J. Yu, B. Su, H. Li, J. Pei, F. H. Sun, M. Zhou, H. Hu, J. W. Li, Z. Han, B. P. Zhang, T. Mori and J. F. Li, *Nat. Commun.*, 2022, **13**, 6087.
- 82 J. Zhou, Z. Chen, J. Luo, W. Li and Y. Pei, *Adv. Mater.*, 2024, **36**, e2405299.
- 83 Y. Qin, B. Qin, T. Hong, X. Zhang, D. Wang, D. Liu, Z. Y. Wang, L. Su, S. Wang, X. Gao, Z. H. Ge and L. D. Zhao, *Science*, 2024, **383**, 1204-1209.



- 84 Y. Zhang, Z. Li, S. Singh, A. Nozariasbmarz, W. Li, A. Genc, Y. Xia, L. Zheng, S. H. Lee, S. K. Karan, G. K. Goyal, N. Liu, S. M. Mohan, Z. Mao, A. Cabot, C. Wolverton, B. Poudel and S. Priya, *Adv. Mater.*, 2023, **35**, e2208994. View Article Online  
DOI: 10.1039/D6EE01515H
- 85 D. Liu, S. Bai, Y. Tian, J. Peng, S. Liu, H. Shi, H. Liang, Y. Qin, L. Su, X. Qian, B. Qin and L. D. Zhao, *Adv. Mater.*, 2025, **37**, e2506999.
- 86 M. T. Agne, K. Imasato, S. Anand, K. Lee, S. K. Bux, A. Zevalkink, A. J. E. Rettie, D. Y. Chung, M. G. Kanatzidis and G. J. Snyder, *Mater. Today Phys.*, 2018, **6**, 83-88.



### Data availability

All data generated or analysed during this study are included in this article (and its supplementary information file).

